OPEN ACCESS

ACTA METALLURGICA SLOVACA

2026, VOL. 32, NO. 2, 74-79

RESEARCH PAPER

Synthesis of $LiMnO_2$-graphene nanoplatelets composite by hydrothermal process

Binh Ngoc Duong[1], Thang Van Pham[1], Hung Tuan Hoang[1], Duong Van Dao[2], Thang Hong Le[1], Huy Duc Tran[1]*

[1]School of Materials Science and Engineering, Hanoi University of Science and Technology, Hanoi, Vietnam
[2]Phenikaa School of Engineering, Phenikaa University, Hanoi, Vietnam

*Corresponding author: binh.duongngoc@hust.edu.vn tel.: 84973002988, School of Materials Science and Engineering, Hanoi University of Science and Technology, Hanoi, Vietnam.

Received: 03.03.2026
Accepted: 19.04.2026

ABSTRACT

The pristine o-$LiMnO_2$ (PL) and in-situ composite samples between o-$LiMnO_2$ and graphene nanoplatelets (GNPs) (L-xGNP with x = 1, 3, 5, 7, 9 wt.% of GNPs) were synthesized successfully via a one-step hydrothermal process. The characterization and electrochemical measurement of the obtained samples were performed. The introduction of GNPs in the L-xGNP composites reduces the growth of primary particles of o-$LiMnO_2$ and provides improved performances as cathode in lithium-ion batteries compared to the PL sample, in which the L-3GNP (3 wt.% GNPs) is the optimal sample amongst the L-xGNP composites with the highest discharge capacities of 151.90 $mAhg^{-1}$ at 0.1 C and 98.46 $mAhg^{-1}$ at 1 C and remained over 94 % of the discharge capacity after 90 cycles. It also exhibited the lowest charge-transfer resistance (72.007 Ω) and the highest electrical conductivity (4.95×10^{-5} $S \cdot cm^{-1}$). The enhanced performance is attributed to improved Li^+ storage capability, reduced electrode volume variation, and suppressed Mn^{3+} dissolution.

Keywords: $LiMnO_2$; graphene; composite.

INTRODUCTION

Due to the global energy scarcity, the high cost and instability of natural green energy sources, and the environmental pollution from fossil-fuel manufacturing, lithium-ion batteries remain among the most sustainable power sources for handheld electronics today. Among base cathode materials, $LiMnO_2$ is notable for its low manufacturing cost, positive environmental impact, low human cost, and high reversible capacity. However, structural instability of layered $LiMnO_2$ during lithiation/delithiation and side reactions between $LiMnO_2$ and electrolytes negatively impact its electrochemical performance, including capacity loss, poor charge/discharge rates, voltage decay, and so on. Therefore, various strategies to enhance its electrochemical performance have been developed, such as doping, coating, defective-structure design, and heterostructure design [1-4].

With high mobility of charge carriers, a unique layered structure, and excellent physicochemical properties, graphene and its derivatives have a great potential in lithium-ion batteries (LIBs) in general, and in $LiMnO_2$ cathode materials in particular. Under hydrothermal conditions, the mechanism of hydrothermal reactions follows the nucleation model in the liquid phase, in which $LiMnO_2$ precursors are dissolved in the solvent to form a supersaturated solution, and stable nucleation begins when supersaturation exceeds the critical threshold [5]. Due to its thermal stability, chemical inertness, and high surface energy, graphene acts as a heterogeneous nucleation surface for $LiMnO_2$ crystals. Furthermore, the high surface energy of graphene can also induce an encapsulating effect, in which $LiMnO_2$ nuclei are wrapped by graphene sheets. It helps hinder the growth of nuclei, resulting in smaller, finer $LiMnO_2$ particles. On the other hand, increasing the graphene content gradually improves the electrical conductivity of composites due to the formation of a conductive network of graphene sheets, transitioning from an electron “hopping” mechanism between isolated graphene sheets to conduction through continuous pathways once the percolation threshold is surpassed [6]. A porous structure can also form between $LiMnO_2$ crystals and graphene, facilitating electrolyte penetration to the cathode’s surface and reducing interfacial resistance between the electrolyte and the cathode, thereby increasing the system's reversible capacity [7]. However, the use of single-layer graphene not only fails to enhance the Li^+ ion storage capacity due to Li-C bond formation that increases the energy of the Li-graphene composite system, but can also lead to the accumulation of Li atoms on the cathode during discharge processes, which promotes dendrite formation and increases the risk of short-circuiting as a result [8]. In contrast, in addition to its quite high specific capacity of 372 mAh g^{-1}, graphite acts as a layered-structure active material that stores Li^+ ions. It not only enhances the theoretical and practical capacities of the composites but also improves the cathode's capacity retention [8]. Therefore, graphene nanoplatelets (GNPs), which are composed of several graphene layers and possess properties intermediate between graphene and graphite, are used as one of the precursors to synthesise the LiMnO2-GNP composites to retain the high Li+ ion storage ability and dendrite-suppressing behaviour of graphite and the superior electrical conductivity of graphene.

In this work, the in-situ $LiMnO_2$-GNP composites were synthesized by hydrothermal process of the precursors $LiOH.H_2O$, Mn_2O_3, and GNPs. Then, the structure, morphology, dispersion, and electrochemical properties of the formed composites were discussed in detail.

MATERIAL AND METHODS

Lithium hydroxide monohydrate ($LiOH.H_2O$), manganese (III) oxide (Mn_2O_3) and graphene nanoplatelets (GNPs) were used as precursors for the fabrication of in-situ $LiMnO_2$-GNP composites. $LiOH.H_2O$ and manganese dioxide (MnO_2) powder were acquired from Macklin, China with a purity of 98% and 99%, respectively. GNPs were acquired from Shanghai Aladdin Biochemical Technology Co., Ltd. with a purity of above 90%. Mn_2O_3 powder was obtained by the calcination of MnO_2 powder at 800 °C for 2 h in air, which was according to the reaction:

$$4MnO_2 = 2Mn_2O_3 + O_2 \quad (1)$$
$$Mn_2O_3 + 2LiOH.H_2O = 2LiMnO_2 + 3H_2O \quad (2)$$
$$GNP + 0{,}5Mn_2O_3 + LiOH.H_2O = LiMnO_2\text{-}GNP + 1{,}5H_2O \quad (3)$$

The formed Mn_2O_3 powder and GNPs were introduced into the $LiOH.H_2O$ aqueous solution in a 25ml Teflon autoclave to perform the hydrothermal process and produce the $LiMnO_2$-GNP composites. The hydrothermal processes were conducted at 180 °C for 8 h with 4M $LiOH.H_2O$ in aqueous solution, 90 % by weight (wt.%) of Mn_2O_3 available for reaction 2, and the change of wt.% of GNPs in the $LiMnO_2$-GNP composites was 1, 3, 5, 7 and 9 wt.%. The composites were denoted L-xGNP where x was wt.% of GNPs. The synthesis of pristine $LiMnO_2$ (PL) was conducted with the same route. The hydrothermal products were filtered and dried at 80 °C for 7 h in air. The experimental processes are illustrated briefly in **Fig. 1**.

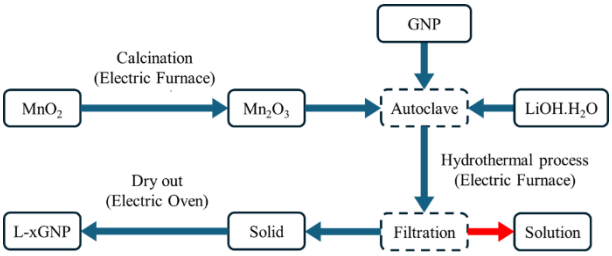

Fig. 1 Schematic diagram of the experimental process

X-ray diffraction analysis (XRD, PANalytical Aeris, Netherlands) was performed to investigate the phase characterization of the powders. Scanning electron microscopy (SEM, JEOL JSM-IT200, Japan) was performed to characterize the morphologies and microstructure of the obtained composites.

The electrochemical performance was examined using CR2032-type coin cells. The working electrodes were obtained by casting homogeneous slurries of the active material (85 wt.%), carbon black (7.5 wt.%, Macklin, China), and sodium carboxymethylcellulose (7.5 wt.%, Xilong Scientific Co., Ltd., China) mixed in distilled water onto aluminum foils and were dried in a vacuum oven at 80 °C overnight. Cell assembly was performed in an argon-filled glove box SG1200/750TS by using the obtained working electrodes as cathode, lithium metal as anode and 1M $LiPF_6$ solution in ethylene carbonate (EC), dimethyl carbonate (DMC) and diethyl carbonate (DEC) (EC/DMC/DEC, 1:1:1 by volume) as electrolyte. The cyclic voltammogram (CV), which was examined over a potential range of 2-4.5 V(Li/Li^+) with scan rate of 0.1 mV s^{-1}, and electrochemical impedance spectroscopy (EIS) with frequency ranging from 10^5 Hz to 0.1 Hz were conducted by using Biologic SP-300. Galvanostatic charge-discharge tests were examined over a potential range of 2-4.7 V(Li/Li^+) using Neware cell testing system.

RESULTS AND DISCUSSION

3.1. Calcination of MnO_2

Fig. 2 shows XRD patterns of the precursor MnO_2 and the product after calcination at 800 °C for 2 hours in air. The peaks in the MnO_2 pattern are indexed to an orthorhombic phase (PDF No. 82-2169); meanwhile, the peaks in the Mn_2O_3 patterns are indexed to a cubic phase (PDF No. 71-0636).

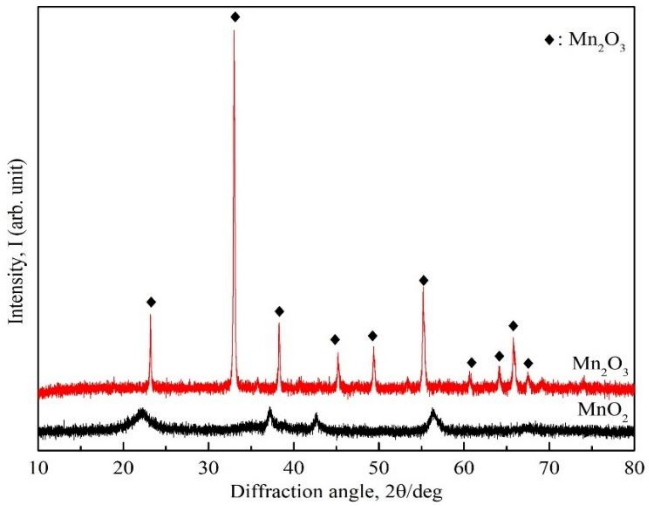

Fig. 2 XRD patterns of precursor MnO_2 and calcinated Mn_2O_3

It can be seen that after calcination at 800 °C, the MnO_2 powders were completely converted to Mn_2O_3. The same result was observed in previous works [9]. For further confirmation, Rietveld analysis was performed for the Mn_2O_3 sample; the results are shown in **Fig 3**.

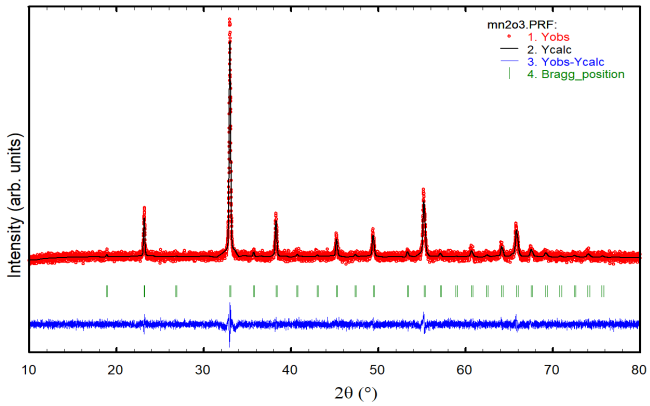

Fig. 3 Rietveld refinement patterns of Mn_2O_3 with observed data (red dots), calculated patterns (black lines), the difference between observed and calculated profiles (blue lines), and Bragg peak positions (green ticks)

Rietveld refinement was conducted by Fullprof Suite software (version 8.00) with crystallographic information files (CIFs) of Mn_2O_3 obtained from Crystallography Open Database (COD). Values of the Chi-Square χ^2, the profile residual R_p, the weighted profile residual R_{wp}, and the expected R-factor R_{exp} are shown in **Table 1**. These factors were defined by the equations shown in the following works [10, 11]. In **Fig. 3**, the observed and computed profiles showed a fairly good fit, indicating that a cubic phase of Mn_2O_3 was obtained from the calcination process.

Table 1. The Chi squared χ^2, the profile residual R_p, the weighted profile residual R_{wp}, and the expected R-factor R_{exp} for Rietveld refinement of Mn_2O_3

Sample	χ^2	R_p	R_{wp}	R_{exp}
Mn_2O_3	1.25	1.65	2.10	1.88

3.2. Synthesis of $LiMnO_2$-GNP composites

Fig. 4 shows the XRD patterns of $LiMnO_2$-GNP composites synthesized at 180 °C for 8 h in aqueous solution of 4M $LiOH.H_2O$. There was 90 wt.% of Mn_2O_3 available for reaction 2. The proportion of GNPs in the composites was varied from
1 to 9 wt.%.

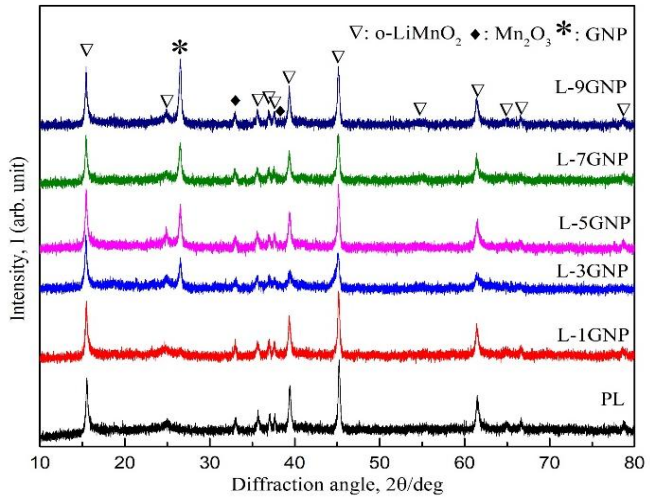

Fig. 4 XRD patterns of a) pristine $LiMnO_2$ and $LiMnO_2$-GNP composites and b) GNPs

The obtained samples are a mixture of orthorhombic $LiMnO_2$ (o-$LiMnO_2$, PDF No. 35-0749), GNPs (PDF No. 41-1487), and Mn_2O_3. Residue of Mn_2O_3 still persist in the samples as its main peaks at 32.9 and 38.3°. Meanwhile, the peak at 26.6° is attributed to GNPs. Formation of o-$LiMnO_2$ crystal is confirmed by Rietveld refinement as shown in **Fig. 5**. Rietveld refinement was also conducted by Fullprof Suite software (version 8.00) with crystallographic information files (CIFs) of GNPs, and $LiMnO_2$ were obtained from Crystallography Open Database (COD). Values of the Chi-Square χ^2, the profile residual R_p, the weighted profile residual R_{wp}, and the expected R-factor R_{exp} are shown in **Table 2**.

Table 2. The Chi squared χ^2, the profile residual R_p, the weighted profile residual R_{wp}, and the expected R-factor R_{exp} for Rietveld refinement of L-3GNP.

Sample	χ^2	R_p	R_{wp}	R_{exp}
L-3GNP	1.15	1.77	2.22	2.08

o-$LiMnO_2$ was also successfully obtained using the same precursors and synthesis route as in our previous work [12]. As seen in **Fig. 4**, the increase of wt.% of GNP in composites barely reduces the formation of o-$LiMnO_2$, which is shown by the intensity variation of o-$LiMnO_2$'s main peaks, i.e. 15.4, 39.3 and 61.3°. The sudden reduction of the formation of o-$LiMnO_2$ in L-3GNP's XRD profile might be due to experimental errors.

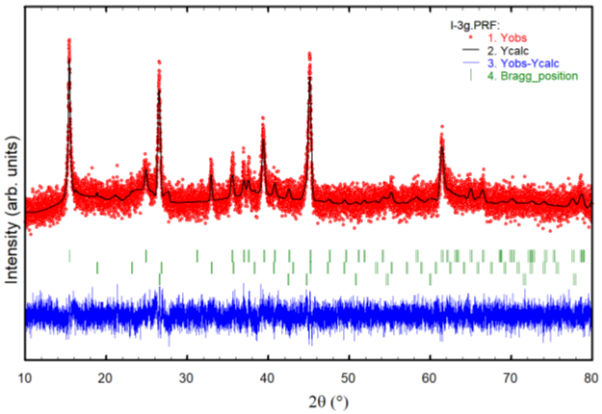

Fig. 5 Rietveld refinement patterns of L-3GNP with observed data (red dots), calculated patterns (black lines), the difference between observed and calculated profiles (blue lines), and Bragg peak positions (green ticks)

Fig. 6 illustrates the SEM images of $LiMnO_2$-GNP composites with different wt.% of GNPs. Crystal growth of o-$LiMnO_2$ should follow the two-dimensional nucleation mechanism and form a layer-by-layer morphology, as observed in **Fig. 6a&c** and discussed in detail in our previous work [12]. **Fig. 6a** also showed the formation of o-$LiMnO_2$ crystals on the GNPs' surface (a darker colour) as a heterogeneous nucleation surface. The encapsulating effect of GNPs on o-$LiMnO_2$ crystals is illustrated in **Fig. 6b**, where $LiMnO_2$ nuclei were formed and wrapped by GNP sheets, which in turn hindered the growth of the nuclei and resulted in finer $LiMnO_2$ particle sizes. A fairly even dispersion of GNPs in composites in shown in **Fig. 6e-h**, even though it is hard to see the distribution of GNPs in the L-1GNP composite in **Fig. 6d**. In the hydrothermal condition with high pressure and a temperature between the usual boiling point 100 °C and the critical temperature 374 °C, i.e. 180 °C in this work, water was superheated; as a result, decreasing viscosity and surface tension of the aqueous solution, increasing solubility and diffusivity of GNPs in water and penetration of water molecules into GNP agglomerates [13]. All these effects, in turn, weakened inter-sheet-van-der-Waals interactions of GNPs and provided sufficient kinetic energy for GNPs to overcome the agglomeration barrier, which caused the deagglomeration and the self-dispersion of GNPs in composites. The primary particle size distribution of o-$LiMnO_2$ in composites is ca. 200-400 nm, although bigger particles could still be observed, meanwhile it is mainly ca. 500 nm-1 µm of pristine o-$LiMnO_2$ as seen in **Fig. 6a&c**, which in turn indicates that the introduction of GNPs formed a network with the role of confining the growth of o-$LiMnO_2$ particle size.

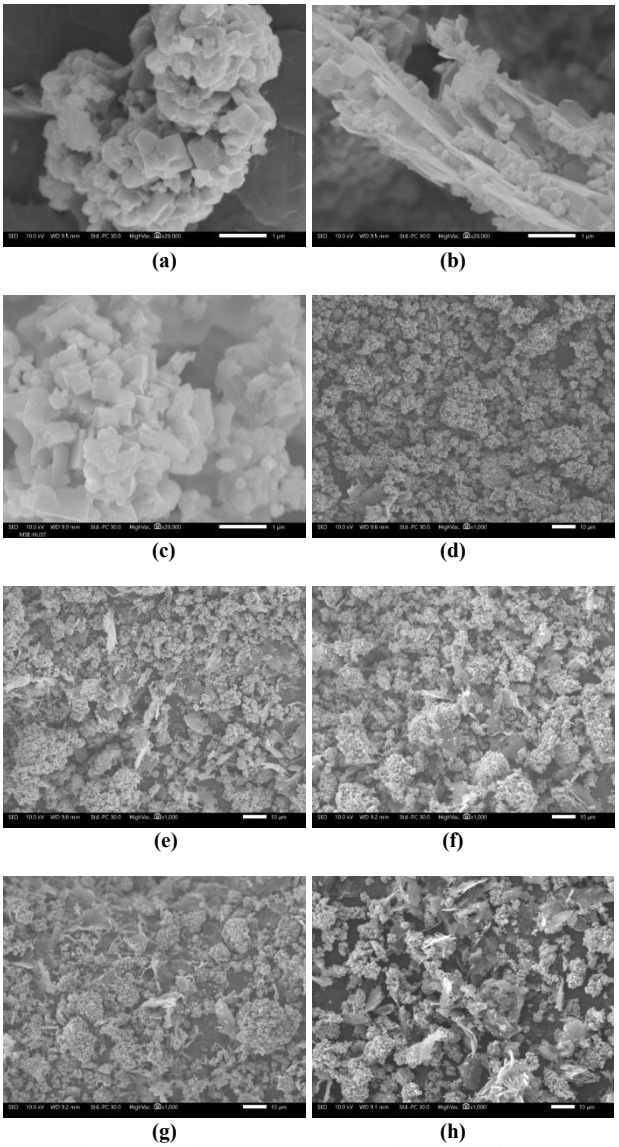

Fig. 6 SEM images of a, b, e) L-3GNP, c) PL, d) L-1GNP, f) L-5GNP, g) L-7GNP, h) L-9GNP

3.3 Electrochemical properties of LiMnO2-GNP composites

The obtained samples LP, L-1GNP, L-3GNP, L-5GNP, L-7GNP, and L-9GNP were investigated by cyclic voltammetry (CV) in the potential range of 2-4.5 V (vs Li/Li^+) at a scan rate of 0.1 mV s^{-1}. The results obtained are shown in **Fig. 7**. As shown in **Fig. 7**, there is one distinct redox pair of peaks located at roughly 3.12-3.14 V for the third cycle and at 3.12–3.2 V for the fifth cycle on charge, and at 2.72-2.81 V for the third cycle and at 2.65-2.79 V for the fifth cycle on discharge. Besides, two pairs of peaks at 4.02-4.18 V for the third cycle and 4.03-4.19 V for the fifth cycle on charge, and at 3.93-4.11 V for the third cycle and 3.95-4.12 V for the fifth cycle on discharge for PL and composite samples are considered the characteristic redox peaks of spinel $LiMn_2O_4$ [14]. The increase of GNP content from 0 to 3 wt.% in composite significantly increases the current magnitude of redox peaks in the fifth cycle, which is because GNPs in composites boost significantly the electronic conductivity and the interaction between the cathodes and the electrolyte, which in turn promote the rate and the

efficiency of electrochemical reactions but also results to form more undesired spinel $LiMn_2O_4$ with more distinct characteristic redox peaks. Previous work also shown a similar trend that the addition of reduced graphene oxide (rGO) in $LiMn_2O_3$/rGO composite increased significantly the formation of spinel phase $LiMn_2O_4$ [14]. Nevertheless, the increase of GNP content from 3 to 9 wt.% in composite reduces considerably the height of redox peaks, which indicates excess GNPs in composite increase diffusion tortuosity of Li ions at the cathode-electrolyte interface and within the bulk composite. The height and size of the redox peaks in **Fig. 7** increase with cycling refer to a progressive formation of spinel phase [15]. Moreover, the potential gaps between redox peaks reduce noticeably with the increase of GNPs content in composites that can be attributed to the improved electronic conductivity and enhanced electrolyte wetting at the cathode-electrolyte interface, which reduce polarization and in turn potentially improve reversibility.

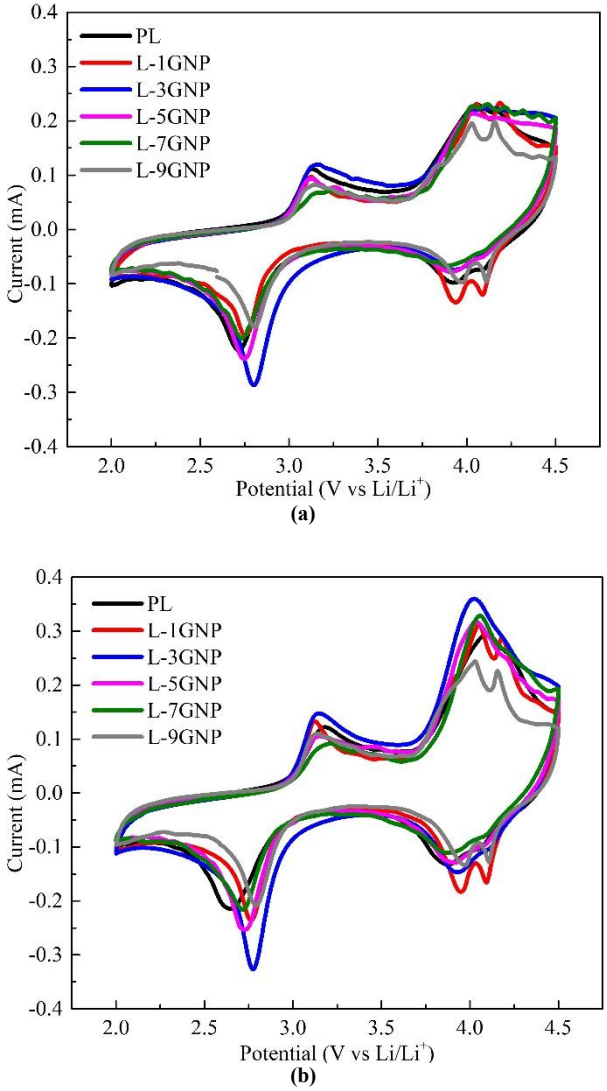

Fig. 7 Cyclic voltammetry curves of PL, L-1GNP, L-3GNP, L-5GNP, L-7GNP and L-9GNP composites with a scan rate of 0.1 mVs-1 for a) the third cycle and b) the fifth cycle

Impedance measurements were performed to understand the effect of GNPs in composite samples, results are shown in **Fig. 8**. As shown in **Fig. 8a** and the inserted image, Nyquist plots show intercepts in the high-frequency range, semicircle-shaped curves in the intermediate frequency range and inclined lines in the low frequency range. The intercepts are assigned to the ohmic impedances (R_S), which represent the battery's ohmic resistances including contributions from electronic current collectors, electrodes, separators, electrolyte and contact resistances [16, 17]. The semicircles correspond to the charge transfer impedance (R_{CT}), including contributions from the cathode electrolyte interphase (CEI) and the electrode polarization impedance [17]. The inclined lines are associated with the impedances or Warburg impedance of Li-ion diffusion in the bulk cathode materials [17].

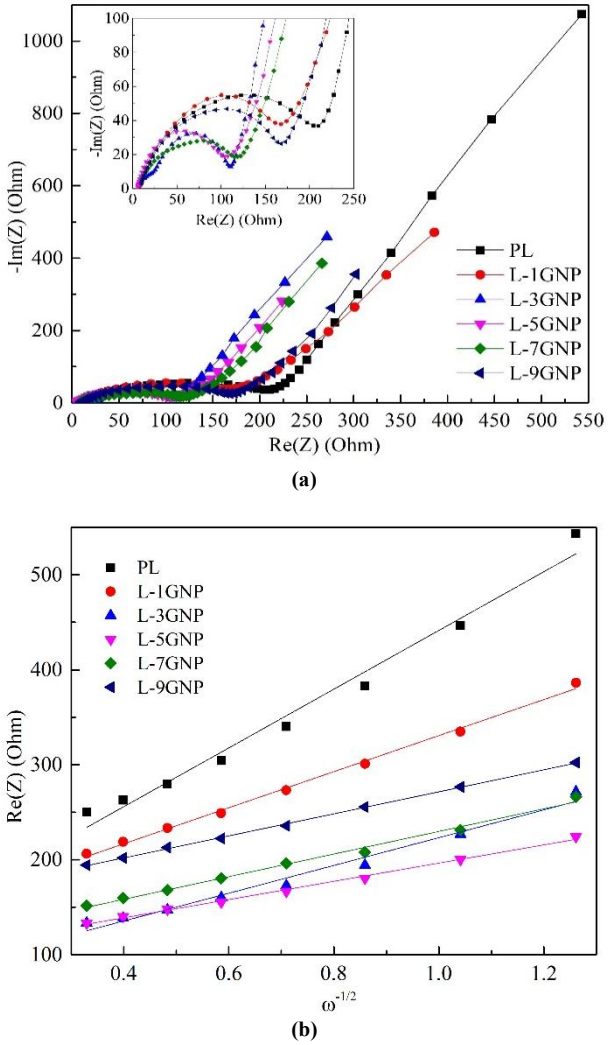

Fig. 8 a) Electrochemical impedance spectroscopy (EIS) with magnified image of EIS profile in the high-to-medium frequency range (inserted image) and b) the relationship between the real part of impedance Re(Z) and the reciprocal square root of angular frequency ω-1/2 in the low frequency range for PL and composite samples

The electronic conductivity (σ_e) can be calculated based on Eq. (4) [18]:

$$\sigma_e = l / (R_{CT} A) \quad (4)$$

where l is the thickness of the cathode material (after subtracting the thickness of the aluminum foil) (cm), R_{CT} is the charge transfer impedance (Ω), and A is the cathode area (cm^2).

The exchange current density (i) and Li-ion diffusion coefficient (D_{Li+}) can be calculated based on Eq. (5) and (6) [19-21]:

$$i = RT / (n F R_{CT}) \quad (5)$$

$$D_{Li+} = R^2 T^2 / (2 A^2 n^4 F^4 C^2 \delta^2) \quad (6)$$

where R is the gas constant 8.314 (J K^{-1} mol^{-1}), T is the Kelvin absolute temperature 298.15 (K), n is the number of transferred electrons per molecular formula, F is Faraday constant 96500 (C mol^{-1}), R_{CT} is the charge transfer impedance (Ω), A is the cathode area (cm^2), C is the concentration of Li-ion in active material (mol cm^{-3}), and δ is the Warburg coefficient which can be drawn from Eq. (7):

$$Re(Z) = R_S + R_{CT} + \delta \omega^{-1/2} \quad (7)$$

where ω is angular frequency in the low frequency range, R_S is the ohmic impedance (Ω), and R_{CT} is the charge transfer impedance (Ω). The fitting results of the real part of impedance Re(Z) and $\omega^{-1/2}$ are shown in **Fig. 8b**.
The electrochemical parameters are drawn from Eq. (4)-(7), and EIS data are shown in **Table 2**.

Table 2 The electrochemical parameters of PL and composite samples calculated and obtained from EIS.

Sample	R_S (Ω)	R_{CT} (Ω)	δ (Ω $S^{1/2}$)	σ_e (S cm^{-1})	D_{Li+} (cm^2 s^{-1})	i (mA cm^{-2})
PL	7.252	124.905	309.248	2.99×10^{-5}	0.607×10^{-16}	0.206
L-1GNP	7.456	133.419	189.792	2.16×10^{-5}	1.613×10^{-16}	0.193
L-3GNP	4.996	72.007	146.203	4.95×10^{-5}	2.718×10^{-16}	0.357
L-5GNP	5.127	95.288	96.025	4.51×10^{-5}	6.300×10^{-16}	0.270
L-7GNP	5.005	105.733	119.053	2.68×10^{-5}	4.099×10^{-16}	0.243
L-9GNP	7.784	147.724	115.992	3.03×10^{-5}	4.318×10^{-16}	0.174

The difference of the ohmic impedance R_S between samples is negligible, while the charge transfer impedance R_{CT} is suppressed significantly from 124.905 to 72.007 Ω as the content of GNPs increases from 0 to 3 wt.%, then the value of R_{CT} increases to 147.724 Ω as the content of GNPs increases to 9 wt.%. The results indicate that GNPs in composite samples not only facilitate the penetration of the electrolyte to the cathode's surface, which increases the contact area between active material particles and the electrolyte, but also provide pathways through the CEI, which in turn reduces the resistance of the Li-ion diffusion through the CEI in the cathode/electrolyte interface. Meanwhile, the exceeded number of GNPs can form barriers that hinder the diffusion of Li-ion in the CEI. The L-3GNP sample shows the most suppressed R_{CT}, which may result in enhanced charge/discharge capacity and improved rate capability. Jo *et al.* [22] also showed a similar trend when comparing pristine $LiMn_2O_4$ with composite samples containing reduced graphene oxide nanosheets. Similar trends are observed in the values of the electronic conductivity σ_e and the exchange current density i, with the highest values obtained from the L-3GNP sample being 4.95×10^{-5} Scm^{-1} and 0.357 $mAcm^{-2}$, respectively, which may lead to better kinetic properties and reduce the polarisation of the electrode system. There is a dramatic increase in the Li-ion diffusion coefficient, D_{Li+}, in the presence of GNPs compared with the PL sample. Unfortunately, the D_{Li+} value of L-3GNP is only 2.718×10^{-16} cm^2 s^{-1} as compared with the highest D_{Li+} 6.300×10^{-16} cm^2 s^{-1} from L-5GNP before decreasing as the amount of GNPs increases further. It suggests that L-5GNP provides the most effective diffusion length for Li ions inside active material particles, which may be attributed to the smaller particle size range by virtue of the wrapping effect of GNPs around o-$LiMnO_2$ and the efficient formation of spinel phases that provide 3D diffusion pathways, which in turn is favorable energetically to the Li-ion diffusion [14].
The initial charge/discharge curves at 0.1 C of the composite samples between o-$LiMnO_2$ and GNPs are displayed in **Fig. 9a**. Two plateaus around 4.0 and 3.0 V in discharge are apparently observed, which show Li ions can intercalate into tetrahedral and octahedral sites, which are associated with the presence of spinel phases and the layered o-$LiMnO_2$ phase, respectively [23, 24]. The initial charge capacity values of L-1GNP, L-3GNP, L-5GNP, L-7GNP and L-9GNP are 140.14, 167.34, 169.30, 157.12 and 159.06 mAh g^{-1}. Meanwhile, L-3GNP exhibits the highest initial discharge capacity, achieving 115.25 mAh g^{-1}, indicating a significant difference relative to the other composite samples and suggesting that L-3GNP may offer better reversibility and reduced irreversible Li-ion consumption. Moreover, L-3GNP shows the longest 3.0 V plateau in discharge compared to the remaining samples, which suggests that 3 wt.% of GNPs is the most effective amount for stabilizing the layered o-$LiMnO_2$ phase. The small plateaus around 4.5 V, which are associated with the deintercalation of Li ions from tetrahedral sites, and the clear plateaus around 3.5-3.7 V, which are associated with the deintercalation of Li ions from octahedral sites, are also observed. The difference between the values of the plateaus in the Li-ion intercalation/deintercalation into/from specific sites is due to the polarization that generally gradually reduces with the increase of the amount of GNPs in composites, which is also observed in **Fig. 7**. The similar polarization-induced effect is displayed in a previous work of Liu and *et al.* [23]. A higher amount of GNPs also improves cycling stability due to the facilitation of electrochemically stable spinel phase, less polarization, and the reduction of cathode volume deformation associated with the intercalation/deintercalation of Li ions and Jahn-Teller distortion, and the suppression of the Mn^{3+} dissolution into the electrolyte, which is observed in **Fig. 9b** [18, 25].

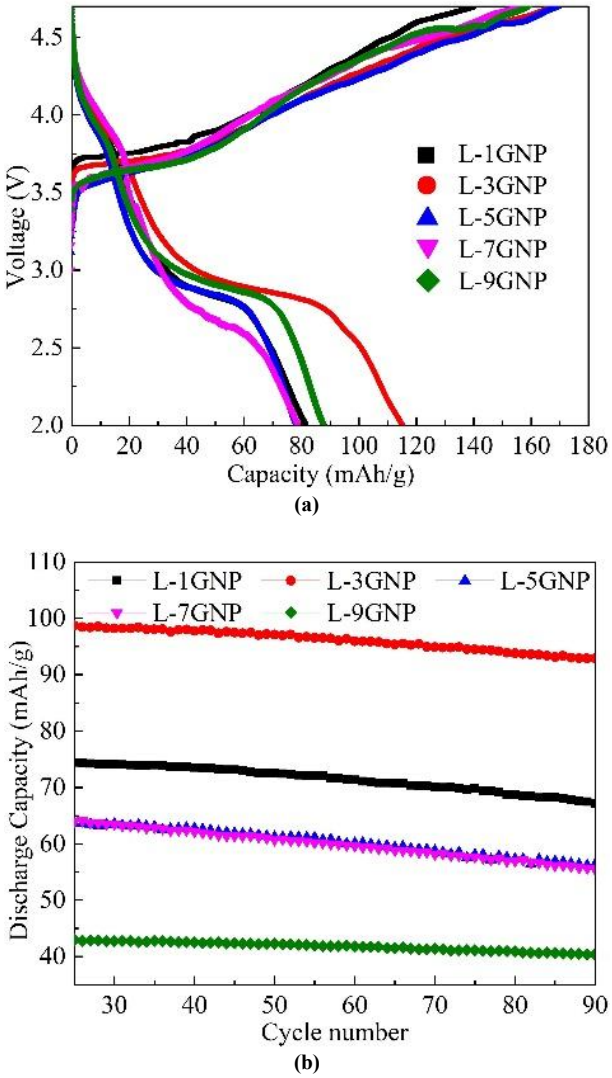

Fig. 9 The electrochemical performance of the composite samples, a) the initial charge/discharge curves at 0.1 C and b) cycle performance at 1 C

Discharge capacity of the composite samples at 0.1 C and 1 C without pre-activating process is shown in **Fig. 10**. The discharge capacities of all samples reduce with the increase of current rate. There are the increases of discharge

capacity of all composite samples in several first cycles that are associated with the activating process, which can be related to the positive layered-to-spinel transformation, the storage of Li ions in GNPs where the *d*-spacing of GNPs increased after each intercalation process, and the improved electrolyte wetting [25-27].

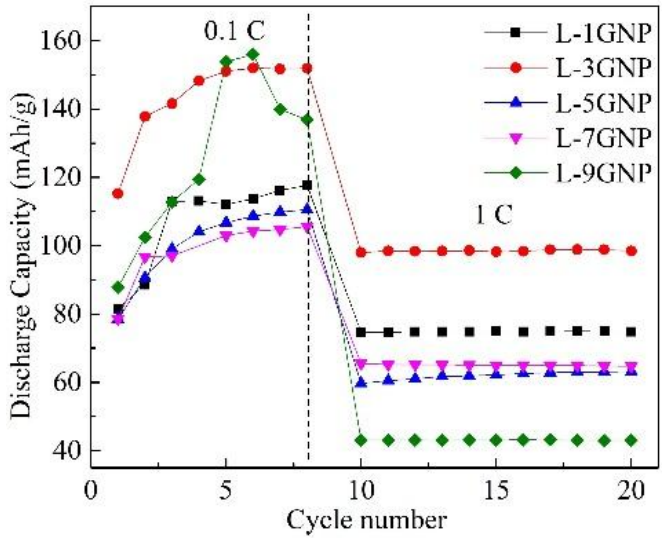

Fig. 10 Rate performance at 0.1 C and 1 C of the composite samples

The L-3GNP composite shows the most stable and highest discharge capacity that achieves 151.90 and 98.46 mAh g^{-1} at 0.1 C and 1 C, respectively. The superior rate performance of L-3GNP can be associated with the minimized charge transfer impedance R_{CT}, which enhances the Li-ion diffusion through the CEI, and the maximized electronic conductivity σ_e and exchange current *i*. Even though having the enhanced Li-ion diffusion coefficients, L-5GNP and L-7GNP show the significantly lower discharge capacities that are roughly 110 and 60 mAh g^{-1} at 0.1 C and 1C, respectively, which can be attributed to the lower R_{CT} and the dilution of o-$LiMnO_2$ in the composite samples. The increase of the stable discharge capacity when increasing the GNP content from 7 to 9 wt.%, which achieve 136.8 mAh g^{-1} at 0.1 C, can be attributed to the Li-ion storability in GNPs and the less polarization. However, the discharge capacity of L-9GNP reduces dramatically to 43.09 mAh g^{-1} at 1 C. It can be that as increasing the current rate, Li-ion storage sites in GNPs are biased toward edges and defects that have both lower energetic barriers and shorter transport pathways rather than within the interlayer spaces between graphene layers [28]. It suggests that at higher current rate, the capacity is increasingly influenced by the charge transfer impedance R_{CT}, the electronic conductivity σ_e and the availability of electrochemically accessible deintercalation/intercalation sites within the active material.

CONCLUSION

The pristine o-$LiMnO_2$ (PL) and *in-situ* composite samples between o-$LiMnO_2$ and graphene nanoplatelets (GNPs) (L-xGNP with x = 1, 3, 5, 7, 9 wt.% of GNPs) were synthesized successfully via a one-step hydrothermal process. The introduction of GNPs in the L-xGNP composites can confine the growth of primary particles of o-$LiMnO_2$, form electronic conductive networks, reduce the cathode volume deformation associated with the intercalation/deintercalation of Li ions, as well as Jahn-Teller distortion and suppress the Mn^{3+} dissolution into the electrolyte during cycling performance, which in turn increases cycling stability of composites. The L-3GNP exhibits the optimal electrochemical performance among the L-xGNP composite samples, with the highest discharge capacities of 151.90 mAh g-1 at 0.1 C and 98.46 mAh g-1 at 1 C, and retains over 94% of its discharge capacity after 90 cycles. The L-3GNP also achieves the lowest charge transfer impedance R_{CT} of 72.007 Ω, the highest electronic conductivity σ_e of 4.95×10^{-5} S cm^{-1} and the highest exchange current density *i* of 0.357 mA cm^{-2} amongst the synthesized samples, even though the improved Li-ion diffusion coefficient D_{Li+} of 2.718×10^{-16} cm^2 s^{-1} is significantly smaller than the highest D_{Li+} of 6.300×10^{-16} cm^2 s^{-1} demonstrated by L-5GNP.

REFERENCES

1. W. He, et al.: Advanced Materials, 33(50), 2021, 2005937. https://doi.org/10.1002/adma.202005937
2. Y. Ma, et al.: Nano Energy, 59, 2019, 184-196. https://doi.org/10.1016/j.nanoen.2019.02.040
3. J. Liu, et al.: Small Methods, 3(12), 2019, 1900350. https://doi.org/10.1002/smtd.201900350
4. Y.P. Deng, et al.: Advanced Functional Materials, 29(19), 2019, 1808522. https://doi.org/10.1002/adfm.201808522
5. P.W. Dunne, et al.: Philosophical Transactions of the Royal Society A: Mathematical, Physical and Engineering Sciences, 373(2057), 2015, 20150015. https://doi.org/10.1098/rsta.2015.0015
6. Y. Wang, J.W. Shan, G. J. Weng: Journal of Applied Physics, 118(6), 2015. https://doi.org/10.1063/1.4928293
7. L. Wang, et al.: Solid State Ionics, 181(37-38), 2010, 1685-1689. https://doi.org/10.1016/j.ssi.2010.09.056
8. Y. Liu, V.I. Artyukhov, M. Liu, A.R. Harutyunyan, B.I. Yakobson: The Journal of Physical Chemistry Letters, 4(10), 2013, 1737-1742. https://doi.org/10.1021/jz400491b
9. O. Fukunaga, K. Takahashi, T. Fujita, J. Yoshimoto: Materials Research Bulletin, 4(5), 1969, pp. 315-322. https://doi.org/10.1016/0025-5408(69)90035-X
10. B.H. Toby: Powder Diffraction, 21(1), 2006, 67-70. https://doi.org/10.1154/1.2179804
11. R.A. Young: *Introduction to the Rietveld method*, Oxford: Oxford Science Publication, 5, 1993, 1-39. https://doi.org/10.1093/oso/9780198555773.003.0001
12. B.N. Duong, T. Van Pham, H.T. Hoang, T.H. Le, H.D. Tran: Acta Metallurgica Slovaca, 30(3), 2024, 127-132. https://doi.org/10.36547/ams.30.3.2061
13. J.M. Lorenzo, P. Putnik, D.B. Kovačević, M. Petrović, P.E. Munekata, B. Gómez, K. Marszałek, S. Roohinejad, F.J. Barba: Studies in Natural Products Chemistry, 64, 2020, 111-130. https://doi.org/10.1016/B978-0-12-817903-1.00004-8
14. W. Zhao, L. Xiong, Y. Xu, H. Li, Z. Ren: Journal of Power Sources, 349, 2017, 11-17. https://doi.org/10.1016/j.jpowsour.2017.03.022
15. E.M. Jin, B. Jin, Y.S. Jeon, K.H. Park, H.B. Gu: Journal of Power Sources, 189(1), 2009, 620-623. https://doi.org/10.1016/j.jpowsour.2008.09.102
16. M.K. Ratib, K.M. Muttaqi, M.R. Islam, D. Sutanto, A.P. Agalgaonkar: International Journal of Hydrogen Energy, 49, 2024, 625-645. https://doi.org/10.1016/j.ijhydene.2023.08.319
17. C. Fan, X. Tian, C. Gu: Batteries, 10(12), 2024, 414. https://doi.org/10.3390/batteries10120414
18. Y. Chen, et al.: Materials Today Advances, 1, 2019, 100001. https://doi.org/10.1016/j.mtadv.2018.12.001
19. S. Yang, H. Song, X. Chen: Electrochemistry Communications, 8(1), 2006, 137-142. https://doi.org/10.1016/j.elecom.2005.10.035
20. P.R. Ilango, K. Prasanna, S.J. Do, Y.N. Jo, C.W. Lee: Scientific Reports, 6(1), 2016, 29826. https://doi.org/10.1038/srep29826
21. D.W. Dees, S. Kawauchi, D.P. Abraham, J. Prakash: Journal of Power Sources, 189(1), 2009, 263-268. https://doi.org/10.1016/j.jpowsour.2008.09.045
22. K.Y. Jo et al.: Electrochimica Acta, 92, 2013, 188–196. https://doi.org/10.1016/j.electacta.2013.01.022
23. Q. Liu, D. Mao, C. Chang, F. Huang: Journal of Power Sources, 173(1), 2007, 538-544. https://doi.org/10.1016/j.jpowsour.2007.03.077
24. I.J. Davidson, R.S. McMillan, J.J. Murray, J.E. Greedan: Journal of Power Sources, 54(2), 1995, 232-235. https://doi.org/10.1016/0378-7753(94)02074-D
25. Y.I. Jang, B. Huang, H. Wang, D.R. Sadoway, Y.M. Chiang: Journal of the Electrochemical Society, 146(9), 1999, 3217. https://doi.org/10.1149/1.1392457
26. J. Guo, Y. Li, J. Meng, K. Pedersen, L. Gurevich, D.I. Stroe: Journal of Energy Chemistry, 74, 2022, 34-44. https://doi.org/10.1016/j.jechem.2022.07.005
27. Y. Sheng: *Investigation of electrolyte wetting in lithium ion batteries: Effects of electrode pore structures and solution,* The University of Wisconsin-Milwaukee, 2015.
28. H. Wu, Q. Liu, S. Guo: Nano-Micro Letters, 6(4), 2014, 316-326. https://doi.org/10.1007/s40820-014-0004-6